# Surface-Orientation-Dependent Distribution of Subsurface Cation-Exchange Defects in Olivine-Phosphate Nanocrystals

**Sung-Yoon Chung,[*,†,⊥] Si-Young Choi,[‡,⊥] Tae-Hwan Kim,[§] and Seongsu Lee[§]**

[†]Graduate School of EEWS, Korea Advanced Institute of Science and Technology (KAIST), Daejeon 305-701, Korea, [‡]Korea Institute of Materials Science, Changwon 641-831, Korea, and [§]Korea Atomic Energy Research Institute, Daejeon 305-353, Korea. [⊥]S.-Y. Chung and S.-Y. Choi contributed equally to this work.

**ABSTRACT** Atomic-scale exchange between two different cations of similar size in crystalline oxides is one of the major types of point defects when multiple cations in oxygen interstitials are arrayed in an ordered manner. Although a number of studies have been performed on a variety of Li-intercalation olivine phosphates to determine the distribution of exchange defects in bulk, understanding of the thermodynamic stability of the defects in subsurface regions and its dependency on the crystallographic orientation at the surface has remained elusive. Through a combination of small-angle neutron scattering, atomic-scale direct probing with scanning transmission electron microscopy, and theoretical *ab initio* calculations, we directly demonstrate that the antisite exchange defects are distributed in a highly anisotropic manner near the surfaces of $LiFePO_4$ crystals. Moreover, a substantial amount of cation exchanges between Li and Fe sites is identified as an energetically favorable configuration in some surface regions, showing excellent agreement with the calculation results of negative defect formation energies. The findings in this study provide insight into developing better ways to avoid degradation of lithium mobility through the surface as well as scientifically notable features regarding the distribution of exchange defects in olivine phosphates.

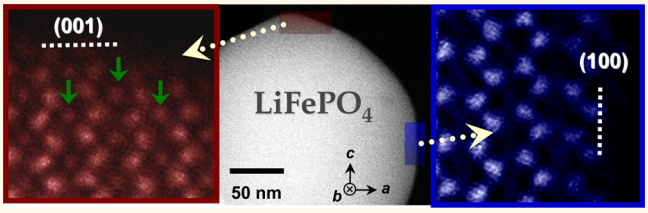


**KEYWORDS:** antisite defects · cation disordering · Li-ion batteries · olivine phosphates · surface · TEM

As local atomic disorder in well-ordered multicomponent crystals has crystallographically asymmetric nature and chemically distinct antisite occupancy, the overall electrical and optical properties and ionic transport behavior of the crystals vary, strongly depending on the distribution and configuration of the disorder in a crystal lattice. Identification of such zero-dimensional defects and subsequent control of their formation have proved to be challenging issues, especially in compound semiconductors,[1−3] metallic alloys,[4,5] oxides with multiple cations,[6,7] and Bi-based chalcogenides.[8−11] In addition to macroscopic concentration determination of atomic disorder from conventional powder diffractions, direct local probing techniques have been widely utilized to detect its microscopic variation in the spatial distribution. Furthermore, substantial progress in imaging science based on scanning probe microscopy (SPM) and transmission electron microscopy (TEM) has made it possible to visualize the precise configuration of atomic disorder in many crystalline solids at atomic resolution. Direct imaging of Mg−Al cation inversion at a spinel-oxide surface by SPM[7] and chemical identification of Bi−Te(Se) antisite defects *via* TEM[10,11] are recent notable examples illustrating the value of atomic-scale observation of point defects.

Lithium-intercalated transition metal oxides that are used as electrode materials in electrochemically rechargeable cells are also relevant crystalline systems that demonstrate the significance of control of cation ordering. Lithium ion diffusion in layer-structured $LiMO_2$ (where M = Co, Mn, and Ni) and olivine-type $LiMPO_4$ (where M = Fe, Mn, and Co) is highly anisotropic.[12−14] Consequently, to attain crystals with a high degree of Li−M ordering and thereby

* Address correspondence to nalphates@gmail.com, sychung@kaist.ac.kr.

Received for review November 14, 2014 and accepted January 7, 2015.

**Published online January 07, 2015**
**10.1021/nn506495x**

achieve enhanced lithium mobility through the diffusion channels, elucidation of the atomistic structure in the thermodynamically stable configuration of local cation disorder and understanding of the kinetic occurrence of cation intermixing during high-temperature synthesis or electrochemical reactions are crucial for real applications.

Since the reports on direct visualization of antisite defects in $LiFePO_4$ (refs15, 16), high-angle annular dark-field (HAADF) scanning transmission electron microscopy (STEM), the image contrast of which is very sensitive to the average atomic number, *Z*, has been extensively used in many other lithium-intercalated metal oxides as an efficient and powerful tool for atomic column-by-column investigations.[17−26] Recent observations of Ni segregation in the Li layer after synthesis of $Li_{1+x}(Mn,Ni)O_2$ crystals,[19] high-voltage cycling-induced intermixing at the surface of $Li_{1+x}(Mn,Ni)O_2$ and $Li(Mn,Ni,Co)O_2$ particles,[21,22] and even nanoscale phase evolution in $FeF_2$ during lithiation[23] from Z-contrast STEM were invaluable findings to correlate structural change with resulting lithium storage performance.

Many theoretical and experimental studies also have been carried out to identify the formation of antisite defects and resulting local cation disorder[27−30] as well as phase transition behavior[31−38] during (de)intercalation reactions in olivine $LiMPO_4$, where the diffusion of uniaxially restricted lithium ions in the lattice varies remarkably with the degree of Li−M ordering. Along with systematic investigations of thermodynamically favorable point defects and intriguing electronic structures *via* density-functional theory (DFT) calculations,[28,39] TEM-based atomic-scale analyses have recently unveiled noteworthy structural details of $LiMPO_4$. These include the peculiar configuration of antisite defects in $LiFePO_4$ and $LiMnPO_4$ (refs 40, 41), the appearance of Li-vacancy staging and its size-dependent behavior in $Li_{1-x}FePO_4$ (refs 42, 43), and the extensive occurrence of disorder after chemical delithiation in $LiCoPO_4$ (ref 44). However, most previous works have focused on the features appearing in the interior of bulk crystals. Few atomic-level studies related to near-surface cation disorder and its dependency on the crystallographic orientation of surfaces in olivine phosphates have been reported, despite that substantial differences in local distributions are expected.

In this study, we demonstrate remarkable orientation-dependent variation in the formation energy and resulting distribution of cation exchange defects near the surface of $LiFePO_4$ crystals. Both small-angle neutron scattering (SANS) for a macroscopic analysis of an entire powder sample and Z-contrast HAADF-STEM for atomic-level probing were utilized to precisely identify the local variation of exchange defects. In addition to direct experimental observations, we theoretically investigated the correlation between the thermodynamic stability of the defects and surface energy at seven major low-index planes by employing *ab initio* DFT calculations. Elucidating structural details on cation disorder in each surface region, the present results provide valuable insight into developing better approaches to avoid degradation of lithium mobility and attain long-term performance in olivine phosphates.

## RESULTS AND DISCUSSION

Before atomic column-by-column scrutiny by Z-contrast STEM, we examined surface regions of $LiFePO_4$ crystals using conventional high-resolution electron microscopy (HREM). As described in the Methods section in detail, all the powder samples used in this work were prepared by annealing at 600 °C for a sufficiently long time, 72 h, to obtain crystals wherein the distribution of antisite defects is thermodynamically at equilibrium. Figure 1 shows HREM images representing four different surface regions. While no abrupt change in the lattice fringe between bulk and surface regions was observed in the case of a (100) surface plane (Figure 1a), pronounced contrast variation could be easily recognized in lattice-fringe images of many other surface regions, as exemplified in Figure 1b−d. It is well-known that lattice fringes in HREM can vary, depending on the specimen thickness in addition to the real atomic potential variation. To exclude the specimen-thickness effect, all of the images were acquired within surface regions, the thickness of which does not change significantly (less than ±20%, examined by electron energy-loss spectra). The depth of surface layers with different contrast ranges from 0.6 to 2.5 nm, and is ∼1.5 nm on average. A geometric phase analysis (GPA)[45] with HREM images revealed that lattice strain has been induced at the surface regions showing distinct contrast variation. Figure 1e shows the GPA results for the region indicated by a yellow rectangle in Figure 1c. These strain maps quantitatively represent the presence of out-of-plane tensile strain ($\varepsilon_{xx}$), whereas no significant in-plane strain ($\varepsilon_{yy}$) is detected. The strain profile for the region denoted by A−B in the $\varepsilon_{xx}$ map directly shows that the maximum out-of-plane lattice dilatation is ∼11.2% in the surface area.

As the surface layers have a different molar volume due to out-of-plane tensile strain, their scattering length density ($\rho_s$) in SANS should differ from that of the interior bulk ($\rho_b$) even though the composition is identical between the bulk and the surface region. Therefore, the overall macroscopic morphology of the surface layers can be efficiently estimated as a distinguishable phase by using SANS.[46] Figure 2 plots the coherently scattered neutron intensities as a function of the magnitude of the scattering wavevector. As can be seen in this plot, the curve fitting (blue curve) to the experimental scattering data (red dots) is accomplished very well when a model function based

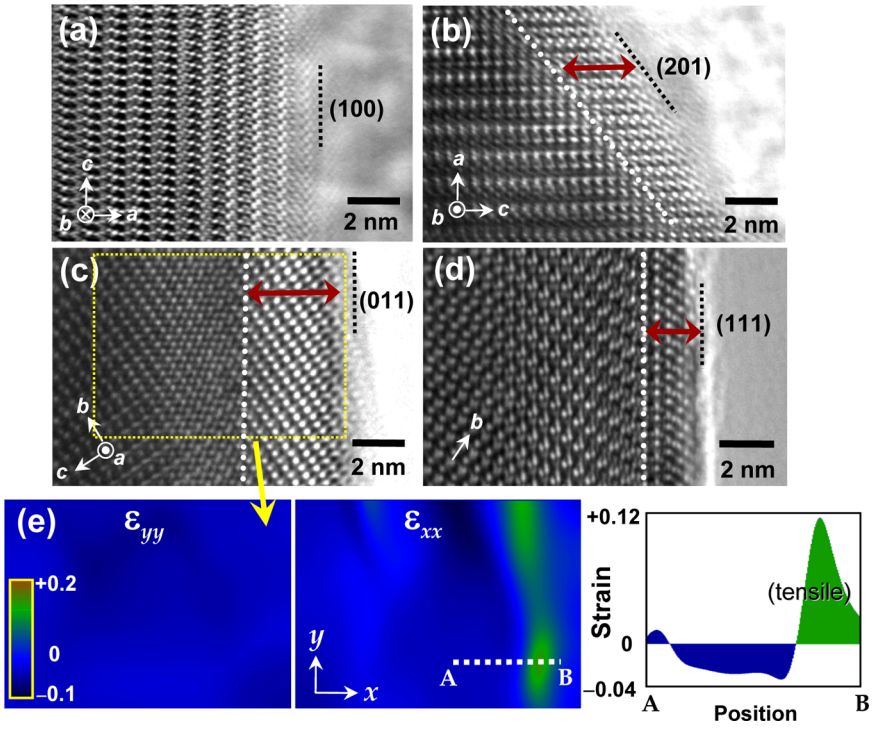


**Figure 1. HREM images of the surface regions in $LiFePO_4$ crystals and GPA results. (a−d) As denoted by red arrows, discrete change in the lattice fringe can be found in the (201), (011), and (111) surface regions, while such notably abrupt variation of the fringe is not observed in the (100) surface region. (e) The strain maps showing out-of-plane ($\varepsilon_{xx}$) and in-plane ($\varepsilon_{yy}$) components are provided for the surface region indicated by a yellow rectangle in (c). Together with the strain profile for the location denoted by A−B in the $\varepsilon_{xx}$ map, these GPA results demonstrate the lattice dilatation largely along the out-of-plane direction in the surface region.**

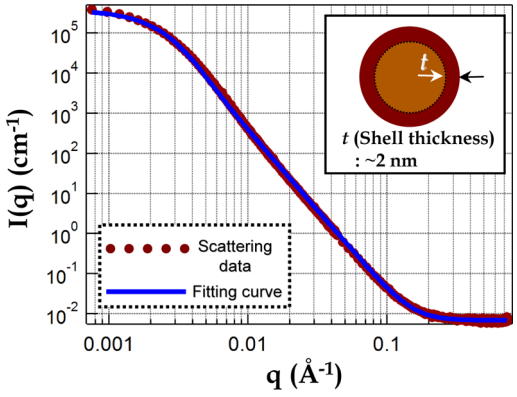


**Figure 2. Intensity profile of coherently scattered small-angle neutrons. When a model function (blue line) based on polydisperse spheres with a shell is applied for data fitting, good agreement with the experimentally obtained scattering data (red dots) is seen.**

on polydisperse spheres[47,48] having a shell of 2 nm average thickness ($t$) is applied. From the values of each scattering length density, $\rho_b$ and $\rho_s$, the volume of the shell is also calculated to be 8.0% larger than that of the bulk (see the SANS results summarized in Table S1 of the Supporting Information). This verifies the volume expansion induced by tensile strain, as demonstrated *via* the GPA results in Figure 1e.

In good agreement with previous experimental observations by HAADF-STEM,[15,16] systematic DFT calculations have recently confirmed that a nearest-bound antisite exchange pair, $Li'_{Fe}$−$Fe^{\bullet}_{Li}$, is energetically the most favorable intrinsic point defect in $LiFePO_4$ at high temperature.[28] In addition, previous neutron powder diffraction results have also shown that the molar volume of crystals expands as the degree of antisite cation disorder in $LiMPO_4$ increases.[30] As a result, it can be easily deduced that the nanometer-thick surface layers observed in the HREM and SANS analyses stem from the presence of a substantial amount of $Li'_{Fe}$−$Fe^{\bullet}_{Li}$ exchange defects segregated near the surface of $LiFePO_4$ crystals. We thus utilized Z-contrast HAADF-STEM in order to directly probe the atomic columns without ambiguity. Figure 3 shows the Z-contrast atomic-column images near a (001) vicinal surface plane denoted by red and purple rectangular shadows, respectively, in the low-magnification STEM image. Significant image intensity in most of the Li columns is detectable in a ~2.5 nm-thick surface region, revealing a considerable amount of antisite exchange defects in the surface region. When the distances between Fe columns are directly measured in the out-of-plane direction in the HAADF-STEM image, as shown in Figure 4, they can be identified to increase in the subsurface layer. Red arrows in Figure 4a indicate the Li columns showing much brighter contrast than others due to a higher concentration of antisite Fe. The intensity profile (Figure 4b) for the Fe columns denoted by 1−7 in the image directly demonstrates a substantial

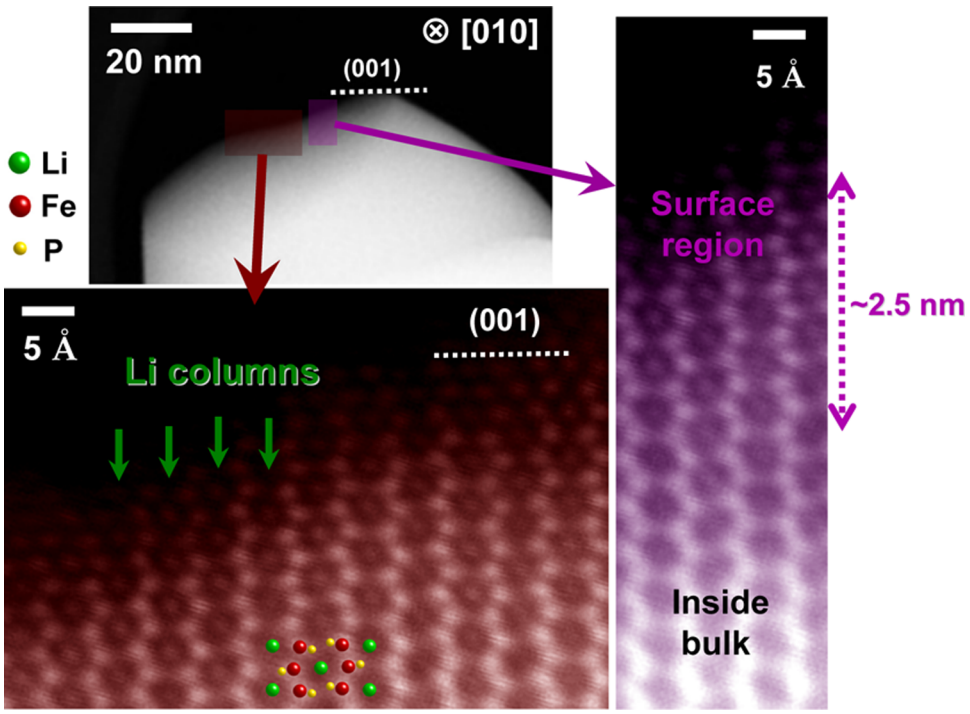


**Figure 3. HAADF-STEM images of the (001) vicinal surface region. The two magnified images for the locations denoted by red and purple shadows in the low-magnification overview image reveal detectable bright intensity in most Li columns (green arrows), demonstrating a substantial amount of Li−Fe exchange defects near the surface. The nanometer-thick surface region is also verified in the purple image.**

increment (>5 Å) in distance between Columns 2−3, 5−6, and 6−7 (denoted by filled red circles). It is also noted that these three pairs of Fe columns are the neighbors of the Li columns with brighter contrast in the image (denoted by the red arrows), strongly supporting the exchange-defect-induced lattice dilatation in agreement with the GPA (Figure 1) and SANS (Figure 2) results.

One of the key findings during the Z-contrast STEM analysis is that high-concentration antisite defects are not observed in every surface region of particles. As already anticipated from the HREM results in Figure 1, observable bright contrast in the Li columns is scarcely detected in some surface regions, indicating a highly anisotropic distribution of exchange defects in subsurface regions. Figure 5 presents a typical example showing remarkable orientation-dependent variation in the subsurface antisite defect concentration. Detectable column intensity in the Li sites is consistently verified in the (001) vicinal subsurface area of a particle, as directly demonstrated by the intensity profile for the Li columns denoted by A−B (green broken line) in the HAADF-STEM image in red. In strong contrast, no such substantial column intensity is observed in the Li sites near the (100) surface, as revealed in the STEM image in blue. Two magnified Z-contrast images for the regions denoted by a white rectangle in each case present an obvious comparison between the two subsurface areas, highlighting the anisotropy in the defect distribution near surfaces.

We performed *ab initio* DFT calculations to theoretically examine the formation energies of an exchange defect pair at various crystallographic surfaces. Seven major low-index surface planes were considered for the calculations. Because a relative comparison of defect formation and its stability between each surface region should be made through this DFT study, two approaches were utilized to construct proper surface-containing supercells for simplicity. First, we adopted a $(LiFePO_4)_x$-type stoichiometric slab with a vacuum layer as a supercell in the same manner as demonstrated in a previous report[49] so that surface atoms with a resulting configuration are simply relaxed without taking complex reconstruction into account. Each surface cut for the seven low-index planes is illustrated in Figure S1 in the Supporting Information. Second, we did not introduce an exchange-defect pair at the topmost surface but did so in the subsurface layers in order to maintain the initial surface termination and thus exclude unknown influence, which may be induced by configuration change at the topmost surface, on the total energy variation of a supercell. For example, as demonstrated in the case of the (010) surface in Figure 6a, a defect pair (pink ellipse) places in the second Li and Fe rows beneath the top surface rather than the very first rows. Other instances of defect-pair arrangement at the remaining six surfaces are also given in Figure 6a. As the initial surface termination is not disturbed by defect introduction in this approach, the relative defect formation energy in each surface region can be reasonably compared with that in the bulk.

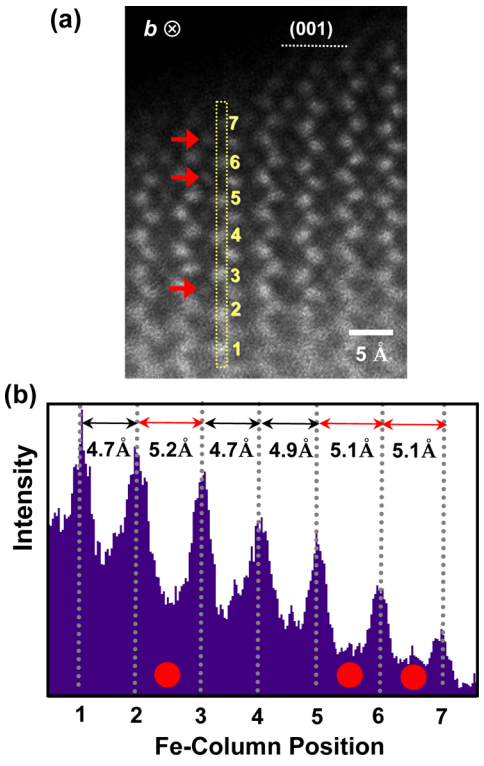


**Figure 4. (a) HAADF-STEM image of the (001) vicinal surface region. Red arrows indicate the Li columns that show much brighter contrast than others due to a higher concentration of antisite Fe. (b) Intensity profile for the Fe columns denoted by 1−7 in the image. As shown in this profile, a substantial increment (>5 Å) in distance between Columns 2−3, 5−6, and 6−7 (denoted by filled red circles) can be identified. It is noted that these three pairs of Fe columns are the neighbors of the Li columns showing brighter contrast in the image, as denoted by the red arrows. Therefore, the exchange-defect-induced lattice dilation is verified in agreement with the GPA and SANS results.**

In fact, there are three geometrically different types of nearest-neighboring Fe for each Li in the $LiFePO_4$ lattice (see Figure S2 in the Supporting Information). Therefore, we calculated the formation energies for all of the three plausible exchange combinations in each subsurface layer (see Table S2 in the Supporting Information) although previous reports have shown that $Li'_{Fe}-Fe^{\bullet}_{Li}$ has the lowest formation energy in the bulk when Li is exchanged with neighboring Fe that locates closest to the Li (Site 1 in Supporting Information Figure S1).[28,41] Table 1 lists the lowest formation energies ($E_S$) of a bound $Li'_{Fe}-Fe^{\bullet}_{Li}$ pair among the three energy values (Supporting Information Table S2) obtained from the DFT calculations for each subsurface layer. Under the present calculation conditions, we also verified again that its formation energy in the bulk ($E_B$) was 0.43 eV, which is consistent with the results in previous reports.[28,41]

The DFT calculation results shown in Table 1 have a few significant implications regarding the formation of antisite defects in the surface regions. First, the defect formation energies considerably vary with crystallographic orientation of surfaces, resulting in highly anisotropic behavior, although they show an overall tendency toward lower values in most of the subsurface layers relative to those in the bulk. For better visualization of this anisotropic feature, an orientation-dependent schematic plot of the defect formation energies is provided in Figure 6b. Second, while the formation energy for a (100) surface is substantially higher than that in the bulk, negative formation energies are obtained for (001) and (111) surfaces, as represented in dark blue colors in Figure 6b. Such negative energy values directly indicate that a certain degree of disorder between Li and Fe sites is thermodynamically stable in both surface layers. As listed in the last column of Table 1, the energy difference, $\Delta E = E_S - E_B$, thus reflects the likelihood of an exchange defect pair forming in the surface region, compared to formation in the bulk. It shows that the more negative the value of $\Delta E$ is, the defect formation accordingly becomes energetically more favorable. In this regard, the DFT calculations exhibit excellent agreement with the Z-contrast STEM observations showing a substantially high concentration of antisite defects for the (001) surface region, in pronounced contrast to scarce detection of defects for the (100) surface region, the $\Delta E$ of which is positive, as shown in Figure 5.

Very recently, Dixit *et al.* also reported a similar facet-dependent subsurface distribution of antisite defects in $Li_{1.2}Ni_{0.175}Mn_{0.525}Co_{0.1}O_2$ particles.[50] Such orientation dependency in defect distribution near surfaces thus does not appear to be limited to olivine phosphates but rather may be a general phenomenon in lithium-intercalated transition-metal oxides with an ordered cation array. This anisotropic aspect can be reasonably understood when the layer-by-layer cation configuration near the surface is taken into account. Figure 7 presents schematic illustrations of the atomic geometry near the (100) and (111) surfaces of $LiFePO_4$. In the case of the (100) surface, each single-cation layer consisting of Li or Fe only is arrayed in an ordered manner along the *z* axis, as indicated by thin white lines in Figure 7a. Consequently, if antisite exchange between Li and Fe occurs in this surface region, substantial geometric perturbation in cation ordering between each layer is induced, thereby resulting in an energetically unfavorable state with a relatively high defect formation energy ($E_S = +0.59$ eV). In contrast, a (111) surface region consists of Li−Fe *mixed* cation layers along the *z*-axis surface projection, as denoted in Figure 7b. Even if Li and Fe are exchanged with each other in a certain layer, such an exchange is not a significant geometric variation within the layer. As a result, the formation of antisite defects is much more easily achieved near the (111) surface, showing even a negative formation energy value ($E_S = -0.70$ eV).

The present study offers noteworthy implications regarding the stability of cation ordering at surfaces of $LiFePO_4$ crystals from a structural viewpoint. As verified

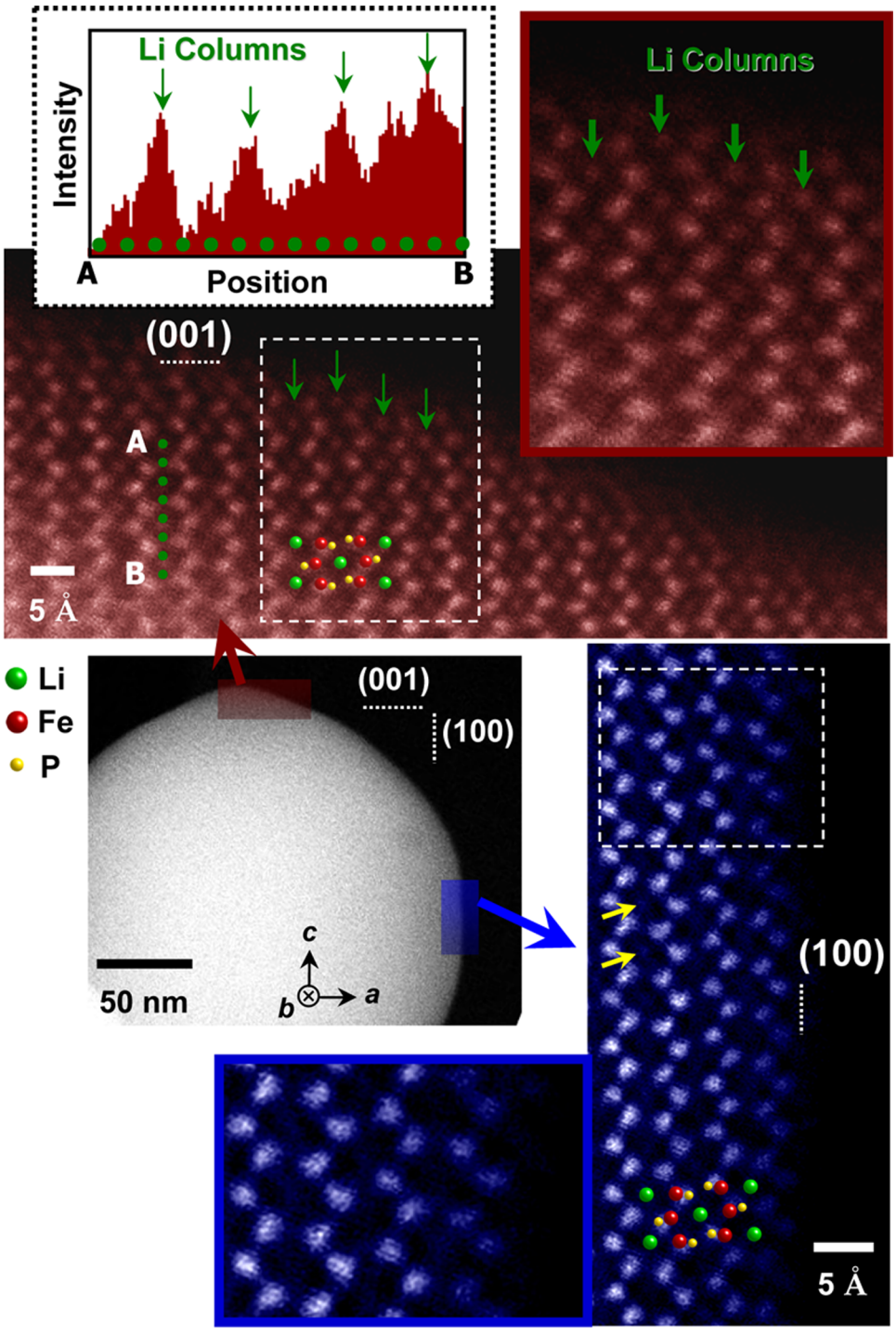


**Figure 5. Comparison between two HAADF-STEM images with different surface orientations. The same image feature of Li columns with detectable intensity is consistently recognized in the (001) vicinal surface regions (in red color). Both the magnified image for the location indicated by a white rectangle and the intensity profile of the Li columns from positions A to B (green broken line) in the red STEM image demonstrate that bright contrast due to antisite Fe ions is observed in most Li columns (green arrows). In the (100) surface region (in blue color), however, such bright Li columns are scarcely observed; only a few Li columns, for example, those denoted by yellow arrows, appear to contain antisite Fe defects. The blue magnification for the location indicated by a white rectangle in the blue STEM image clearly reveals a high degree of cation ordering between Li and Fe sites near the (100) surface.**

by SANS in Figure 2, for long-term application it appears thermodynamically unavoidable that surface layers having low defect formation energies in the end will contain a substantial amount of antisite exchange defects even if the initially obtained crystals immediately after synthesis are free of surface defects. Therefore, the anisotropic nature of the defect distribution should be properly utilized to suppress the degradation

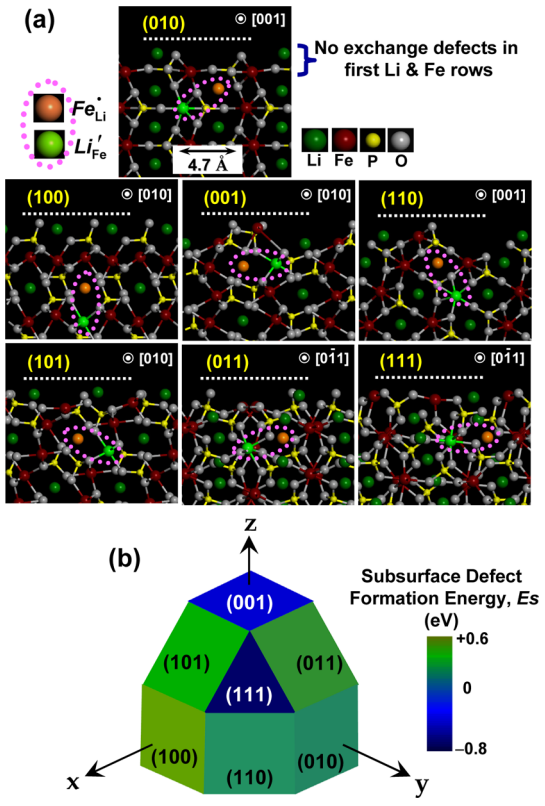


Figure 6. Supercell models for DFT calculations and a graphic diagram of orientation-dependent defect formation energies. (a) An exchange defect pair, as denoted by a pink ellipse, has been introduced in the subsurface layer instead of the top surface to maintain the initial atomic termination in each slab of the seven supercells with different surface orientations. (b) The formation energies of an exchange defect pair in each subsurface layer are graphically displayed, revealing the highly anisotropic characteristics of the local distribution.

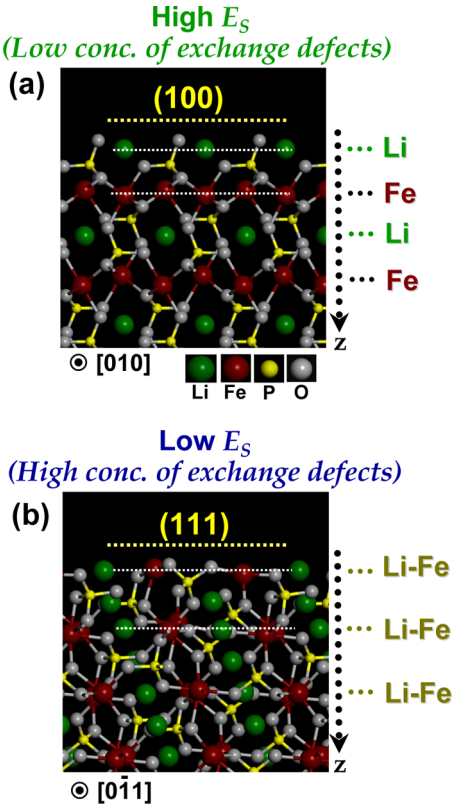


Figure 7. Side views of atomic geometry near (100) and (111) surfaces. (a) A well-ordered stacking sequence in the cation layers (Li–Fe–Li–Fe) along the *z*-axis can be identified in the (100) surface region, as denoted by thin white lines. On the basis of the DFT calculations in Table 1, the high subsurface defect formation energy ($E_S$) is noted. (b) In contrast, the cation layers (thin white lines) along the *z*-axis are composed of a Li–Fe mixture in the (111) surface region. Therefore, even if antisite exchange defects occur in the layer, they are not significant geometric perturbations in the Li–Fe mixture layer, resulting in the much easier defect formation with a very low $E_S$ near the (111) surface.

**TABLE 1. Formation Energies of an Antisite Defect Pair in Each Subsurfaece Layer and Differences ($\Delta E$) with Its Formation Energy in the Bulk[a]**

| Surface Plane | Defect Formation Energy, $E_S$ (eV) | $\Delta E = E_S - E_B$ (eV) |
|---|---|---|
| (100) | 0.59 | 0.16 |
| (010) | 0.14 | –0.29 |
| (001) | –0.56 | –1.03 |
| (110) | 0.15 | –0.28 |
| (101) | 0.38 | –0.05 |
| (011) | 0.25 | –0.18 |
| (111) | –0.70 | –1.13 |

[a] Defect formation energy in bulk, $E_B$: 0.43 eV. The formation energy in red denotes a larger value than the formation energy in bulk (0.43 eV). The negative formation energies are also represented in blue.

of unidirectional lithium-ion mobility by antisite iron ions along the *b* axis through surfaces in $LiFePO_4$.

Four surface planes, (010), (110), (011), and (111), out of the seven listed in Table 1 have a *b*-direction component in their surface normal vectors, thereby being active surface facets for fast lithium diffusion during (de)intercalation reaction. As the (111) surface among these four shows a highly negative value in defect formation energy (−0.70 eV), its development should be suppressed during particle synthesis. The (010) and (110) surfaces also have fairly low defect formation energies (0.14 and 0.15 eV, respectively). Consequently, the findings of the present study strongly imply that plate-type particles with (010) surface facets would not be beneficial for the long-term maintenance of lithium mobility despite remarkable Li-intercalation efficiency through the surface right after particle synthesis.[51] In this regard, the development of (011) surface facets, the defect formation energy (0.25 eV) of which is nearly 2-fold higher than that of a (010) surface, is suggested for better sustainability of rapid lithium motion through the surfaces, although complete suppression of Li–Fe exchange disorder is not attainable even in the (011) surface region, as already shown in the HREM image of Figure 1c.

## CONCLUSION

By a combination of conventional HREM, macroscopic SANS, and Z-contrast HAADF-STEM, we have revealed the presence of surface layers that contain a substantial amount of antisite exchange $Li'_{Fe}$—$Fe^{\bullet}_{Li}$ defects on $LiFePO_4$ crystals as an equilibrium configuration. During atomic column-by-column observations, we also identified that the distribution of the exchange defects is highly anisotropic, providing direct evidence of remarkable variation in their concentration with the crystallographic orientation of surface planes. The formation energies of an exchange defect pair obtained by *ab initio* DFT calculations consistently support this anisotropic aspect of the defect distribution in the surface regions. As our study demonstrates an energetically stable configuration of exchange defects near surfaces, development of surface facets with relatively higher defect formation energies during particle synthesis is reasonably suggested from a structural viewpoint in order to avoid retardation of lithium mobility by antisite iron for long-term utilization of $LiFePO_4$.

## METHODS

**Sample Preparation.** $LiFePO_4$ polycrystals were prepared through a solid-state reaction by using high-purity lithium carbonate ($Li_2CO_3$, Aldrich), iron oxalate dihydrate ($Fe(II)C_2O_4 \cdot 2H_2O$, Aldrich), and ammonium dihydrogen phosphate ($NH_4H_2PO_4$, Aldrich). Stoichiometric powder mixtures of the three starting materials were ball-milled in acetone for 24 h with zirconia milling media. A dried slurry was first calcined at 350 °C for 5 h under a flow of high-purity Ar (99.999%, 400 sccm) to avoid oxidation of the Fe(II). The calcined amorphous powder samples were further annealed at 600 °C in the same Ar atmosphere for a sufficiently long time, 72 h, to obtain crystalline particles having a thermodynamic equilibrium state of defect configurations.

**SANS.** Small-angle neutron scattering measurements were carried out using the 40 m SANS beamline at the HANARO cold neutron facility of the Korea Atomic Energy Research Institute (Daejeon, Korea). Neutron sources of two different wavelengths ($\lambda$) with $\Delta\lambda/\lambda = 0.12$ were used during measurements; $\lambda = 6$ Å for sample-to-detector distances of 1.16 and 5.75 m and $\lambda = 7.49$ Å for the distance of 19.85 m, respectively. Therefore, the magnitude of the scattering wavevector ($q = (4\pi/\lambda)\sin\theta$, where $\theta$ is the scattering angle) ranges from 0.0007 to 0.74 Å$^{-1}$. The scattering intensities were corrected for the background, empty cell scattering, and sensitivity of the individual detector pixcels, and their corrected data sets were placed on an absolute scale. Among many available model functions embedded in the IGOR Pro software for diverse form factors, a model based on polydisperse core—shell spheres was adopted for data fitting. As previously reported in detail,[47] the single particle amplitude, $F(q)$, which correlates with a corresponding form factor, in this core—shell sphere model is given as follows.

$$\frac{d\Sigma}{d\omega}(q) = nF(q)^2 \quad (1)$$

$$F(q) = 4\pi \int r^2[\rho(r) - \rho_m]\frac{\sin qr}{qr}dr \quad (2)$$

$$\rho(r) = \rho_c(r \leq r_c) \text{ and } \rho_s(r_c < r \leq r_c + t) \quad (3)$$

where $d\Sigma/d\omega$ is the macroscopic differential cross section per unit volume, which is proportional to the directly measured intensity in a scattering experiment, $n$ is the number density of spheres, $\rho(r)$ is the scattering length density (SLD) with a spherically symmetric profile as a function of the radius ($r$), $\rho_m$ is the SLD of the medium (air in our case), $\rho_c$ is the SLD of the spherical core of radius $r_c$, and $\rho_s$ is the SLD of the shell with a constant thickness of $t$. In addition, the SLD in small-angle scattering is defined as

$$\rho = \frac{\sum_i^n b_i}{V} \quad (4)$$

where $b_i$ is the scattering length of the relevant atom and $V$ is the volume containing $n$ atoms. As a result, if a sufficient volume difference is present between the core and the shell of particles, it leads to substantial variations in the SLD of each region, making the core—shell morphology effectively distinguishable by SANS.

**HREM, GPA, and HAADF-STEM.** Conventional phase-contrast HREM images were obtained using a transmission electron microscope (JEM-2100F, JEOL) at 200 kV. The obtained raw images were filtered to eliminate background noises (2D Difference Filters, HREM Research Inc.). A geometric phase analysis, using GPA Phase (HREM Research, Inc.), was performed with HREM images to quantitatively measure small displacements and resulting strain fields induced by lattice misfit between the surface region and the interior bulk. In this analysis, the two-dimensional displacement field can be obtained from the relative phase shifts of a particular set of noncollinear Fourier components in the HREM image (see ref 45 for more details). Z-dependent HAADF images were also obtained using the same transmission electron microscope with a spherical-aberration corrector (CEOS GmbH) for an electron probe. The size of the probe in STEM mode was 0.96 Å. The collection semiangles of the HAADF detector were adjusted from 71 to 190 mrad in order to exploit incoherently scattered electrons at large angles for Z-sensitive images. The obtained raw images were band-pass filtered to reduce background noise.

**DFT Calculations.** *Ab initio* calculations were performed within the spin-polarized generalized-gradient approximation (GGA) along with the Perdew—Burke—Ernzerhof (PBE) functional for exchange correlation and the ultrasoft pseudopotentials for ionic cores, as implemented in the CASTEP code (MS ver. 6.1, Accelrys, Inc.). A sufficiently long slab along with a 10-Å vacuum layer was constructed as an optimum supercell for each calculation to make the relaxation layer of each slab more than 10 Å in thickness. A previously suggested approach based on a stoichiometric slab was adopted for reasonable determination of the surface termination (see ref 49 for details). To exclude any energy variation induced by change of the surface termination, a pair of Li—Fe exchange defects was introduced into the second Li and Fe rows beneath the topmost surface plane, preserving the initial surface termination. The formation energy of a defect pair in the subsurfaece layer ($E_S$) was obtained by

$$E_S = E(\text{defects}) - E(\text{w/t defects})$$

where $E$(defects) and $E$(w/t defects), respectively, are the total energies of a supercell with and without a defect pair after geometry optimization. The plane-wave basis set for the kinetic energy cutoff was 450 eV. Optimization of the internal coordinates for each case was performed using the BFGS algorithm with convergence tolerances of 0.1 eV/Å for the maximum ionic force, $5 \times 10^{-5}$ eV/atom for the total energy, and 0.005 Å for the maximum ionic displacement.

*Conflict of Interest:* The authors declare no competing financial interest.

*Acknowledgment.* This work was supported by the National Research Foundation of Korea (NRF), Grants No. 2014R1A4A1003712 (BRL Program), 2013R1A1A2005243, and 2010-0028973. S.-Y. Choi was also financially supported by the Global Frontier R&D Program (Grant No. 2013M3A6B1078872) on Center for Hybrid Interface Materials. The SANS analysis was supported by HANARO Center of the Korea Atomic Energy Research Institute (KAERI) through the National Nuclear Technology Program.

*Supporting Information Available:* Additional tables for SANS and DFT calculation results, and schematic illustrations for surface cuts and surface facets. This material is available free of charge *via* the Internet at http://pubs.acs.org.

## REFERENCES AND NOTES


1. Zhang, S. B.; Chadi, D. J. Cation Antisite Defects and Antisite-Interstitial Complexes in Gallium Arsenide. *Phys. Rev. Lett.* **1990**, *64*, 1789–1792.
2. Hogan, C.; Magri, R.; Del Sole, R. Spontaneous Formation of Surface Antisite Defects in the Stabilization of the Sb-Rich GaSb(001) Surface. *Phys. Rev. Lett.* **2010**, *104*, 157402.
3. Chen, S.; Walsh, A.; Gong, X.-G.; Wei, S.-H. Classification of Lattice Defects in the Kesterite $Cu_2ZnSnS_4$ and $Cu_2ZnSnSe_4$ Earth-Abundant Solar Cell Absorbers. *Adv. Mater.* **2013**, *25*, 1522–1539.
4. Pourovskii, L. V.; Ruban, A. V.; Johansson, B.; Abrikosov, I. A. Antisite-Defect-Induced Surface Segregation in Ordered NiPt Alloy. *Phys. Rev. Lett.* **2003**, *90*, 026105.
5. Kramer, M. J.; Mendelev, M. I.; Napolitano, R. E. *In Situ* Observation of Antisite Defect Formation during Crystal Growth. *Phys. Rev. Lett.* **2010**, *105*, 245501.
6. Muñoz-García, A. B.; Pavone, M.; Carter, E. A. Effect of Antisite Defects on the Formation of Oxygen Vacancies on $Sr_2FeMoO_6$: Implications for Ion and Electron Transport. *Chem. Mater.* **2011**, *23*, 4525–4536.
7. Rasmussen, M. K.; Foster, A. S.; Hinnemann, B.; Canova, F. F.; Helveg, S.; Meinander, K.; Martin, N. M.; Knudsen, J.; Vlad, A.; Lundgren, E.; *et al.* Stable Cation Inversion at the $MgAl_2O_4$(001) Surface. *Phys. Rev. Lett.* **2011**, *107*, 036102.
8. Scanlon, D. O.; King, P. D. C.; Singh, R. P.; de la Torre, A.; McKeown Walker, S.; Balakrishnan, G.; Baumberger, F.; Catlow, C. R. A. Controlling Bulk Conductivity in Topological Insulators: Key Role of Antisite Defects. *Adv. Mater.* **2012**, *24*, 2154–2158.
9. Peranio, N.; Winkler, M.; Dürrschnabel, M.; König, J.; Eibl, O. Assessing Antisite Defects and Impurity Concentrations in $Bi_2Te_3$ Based Thin Films by High-Accuracy Chemical Analysis. *Adv. Funct. Mater.* **2013**, *23*, 4969–4976.
10. Huang, F.-T.; Chu, M.-W.; Kung, H. H.; Lee, W. L.; Sankar, R.; Liou, S.-C.; Wu, K. K.; Kuo, Y. K.; Chou, F. C. Nonstoichiometric Doping and Bi Antisite Defect in Single Crystal $Bi_2Se_3$. *Phys. Rev. B* **2012**, *86*, 081104(R).
11. Jiang, Y.; Wang, Y.; Sagendorf, J.; West, D.; Kou, X.; Wei, X.; He, L.; Wang, K. L.; Zhang, S.; Zhang, Z. Direct Atom-by-Atom Chemical Identification of Nanostructures and Defects of Topological Insulators. *Nano Lett.* **2013**, *13*, 2851–2856.
12. Thomas, M. G. S. R.; Bruce, P. G.; Goodenough, J. B. Lithium Mobility in the Layered Oxide $Li_{1-x}CoO_2$. *Solid State Ionics* **1985**, *17*, 13–19.
13. Morgan, D.; Van der Ven, A.; Ceder, G. Li Conductivity in $Li_xMPO_4$ (M = Mn, Fe, Co, Ni) Olivine Materials. *Electrochem. Soild-State Lett.* **2004**, *7*, A30–A32.
14. Nishimura, S.-I.; Kobayashi, G.; Ohoyama, K.; Kanno, R.; Yashima, M.; Yamada, A. Experimental Visualization of Lithium Diffusion in $Li_xFePO_4$. *Nat. Mater.* **2008**, *7*, 707–711.
15. Chung, S.-Y.; Choi, S.-Y.; Yamamoto, T.; Ikuhara, Y. Atomic-Scale Visualization of Antisite Defects in $LiFePO_4$. *Phys. Rev. Lett.* **2008**, *100*, 125502.
16. Chung, S.-Y.; Choi, S.-Y.; Yamamoto, T.; Ikuhara, Y. Orientation-Dependent Arrangement of Antisite Defects in Lithium Iron(II) Phosphate Crystals. *Angew. Chem., Int. Ed.* **2009**, *48*, 543–546.
17. Bareño, J.; Lei, C. H.; Wen, J. G.; Kang, S.-H.; Petrov, I.; Abraham, D. P. Local Structure of Layered Oxide Electrode Materials for Lithium-Ion Batteries. *Adv. Mater.* **2010**, *22*, 1122–1127.
18. Javis, K. A.; Deng, Z.; Allard, L. F.; Manthiram, A.; Ferreira, P. J. Atomic Structure of a Lithium-Rich Layered Oxide Material for Lithium-Ion Batteries: Evidence of a Solid Solution. *Chem. Mater.* **2011**, *23*, 3614–3621.
19. Gu, M.; Belharouak, I.; Genc, A.; Wang, Z.; Wang, D.; Amine, K.; Gao, F.; Zhou, G.; Thevuthasan, S.; Baer, D. R.; *et al.* Conflicting Roles of Nickel in Controlling Cathode Performance in Lithium Ion Batteries. *Nano Lett.* **2012**, *12*, 5186–5191.
20. Gu, M.; Belharouak, I.; Zheng, J.; Wu, H.; Xiao, J.; Genc, A.; Amine, K.; Thevuthasan, S.; Baer, D. R.; Zhang, J.-G.; *et al.* Formation of the Spinel Phase in the Layered Composite Used in Li-Ion Batteries. *ACS Nano* **2013**, *7*, 760–767.
21. Xu, B.; Fell, C. R.; Chi, M.; Meng, Y. S. Identifying Surface Structure Changes in Layered Li-Excess Nickel Manganese Oxides in High Voltage Lithium Ion Batteries: A Joint Experimental and Theoretical Study. *Energy Environ. Sci.* **2011**, *4*, 2223–2233.
22. Lin, F.; Markus, I. M.; Nordlund, D.; Weng, T.-C.; Asta, M. D.; Xin, H. L.; Doeff, M. M. Surface Reconstruction and Chemical Evolution of Stoichiometric Layered Cathode Materials for Lithium-Ion Batteries. *Nat. Commun.* **2014**, *5*, 3529.
23. Wang, F.; Yu, H.-C.; Chen, M.-H.; Wu, L.; Pereira, N.; Thornton, K.; Van der Ven, A.; Zhu, Y.; Amatucci, G. G.; Graetz, J. Tracking Lithium Transport and Electrochemical Reactions in Nanoparticles. *Nat. Commun.* **2012**, *3*, 1201.
24. Lu, X.; Sun, Y.; Jian, Z.; Xiaoqing, H.; Gu, L.; Hu, Y.-S.; Li, H.; Wang, Z.; Chen, W.; Duan, X.; *et al.* New Insight into the Atomic Structure of Electrochemically Delithiated O3-$Li_{(1-x)}CoO_2$ ($0 \leq x \leq 0.5$) Nanoparticles. *Nano Lett.* **2012**, *12*, 6192–6197.
25. Boulineau, A.; Simonin, L.; Colin, J.-F.; Bourbon, C.; Patoux, S. First Evidence of Manganese−Nickel Segregation and Densification upon Cycling in Li-Rich Layered Oxides for Lithium Batteries. *Nano Lett.* **2013**, *13*, 3857–3863.
26. Sun, Y.; Zhao, L.; Pan, H.; Lu, X.; Gu, L.; Hu, Y.-S.; Li, H.; Armand, M.; Ikuhara, Y.; Chen, L.; *et al.* Direct Atomic-Scale Confirmation of Three-Phase Storage Mechanism in $Li_4Ti_5O_{12}$ Anodes for Room-Temperature Sodium-Ion Batteries. *Nat. Commun.* **2013**, *4*, 1870.
27. Gardiner, G. R.; Islam, M. S. Antisite Defects and Ion Migration in the $LiFe_{0.5}Mn_{0.5}PO_4$ Mixed-Metal Cathode Material. *Chem. Mater.* **2010**, *22*, 1242–1248.
28. Hoang, K.; Johannes, M. Tailoring Native Defects in $LiFePO_4$: Insights from First-Principles Calculations. *Chem. Mater.* **2011**, *23*, 3003–3013.
29. Malik, R.; Burch, D.; Bazant, M.; Ceder, G. Particle Size Dependence of the Ionic Diffusivity. *Nano Lett.* **2010**, *10*, 4123–4127.
30. Chung, S.-Y.; Kim, Y.-M.; Lee, S.; Oh, S. H.; Kim, J.-G.; Choi, S.-Y.; Kim, Y.-J.; Kang, S.-J. L. Cation Disordering by Rapid Crystal Growth in Olivine-Phosphate Nanocrystals. *Nano Lett.* **2012**, *12*, 3068–3073.
31. Meethong, N.; Huang, H.-Y. S.; Speakman, S. A.; Carter, W. C.; Chiang, Y.-M. Strain Accommodation during Phase Transformations in Olivine-Based Cathodes as a Materials Selection Criterion for High-Power Rechargeable Batteries. *Adv. Funct. Mater.* **2007**, *17*, 1115–1123.
32. Bai, P.; Cogswell, D. A.; Bazant, M. Z. Suppression of Phase Separation in $LiFePO_4$ Nanoparticles during Battery Discharge. *Nano Lett.* **2011**, *11*, 4890–4896.
33. Cogswell, D. A.; Bazant, M. Z. Coherency Strain and the Kinetics of Phase Separation in $LiFePO_4$ Nanoparticles. *ACS Nano* **2012**, *6*, 2215–2225.
34. Sharma, N.; Guo, X.; Du, G.; Guo, Z.; Wang, J.; Wang, Z.; Peterson, V. K. Direct Evidence of Concurrent Solid-Solution and Two-Phase Reactions and the Nonequilibrium Structural Evolution of $LiFePO_4$. *J. Am. Chem. Soc.* **2012**, *134*, 7867–7873.
35. Liu, X.; Liu, J.; Qiao, R.; Yu, Y.; Li, H.; Suo, L.; Hu, Y.-S.; Chuang, Y.-D.; Shu, G.; Chou, F.; *et al.* Phase Transformation and

Lithiation Effect on Electronic Structure of $Li_xFePO_4$: An In-Depth Study by Soft X-ray and Simulations. *J. Am. Chem. Soc.* **2012**, *134*, 13708–13715.
36. Chueh, W. C.; Gabaly, F. E.; Sugar, J. D.; Bartelt, N. C.; McDaniel, A. H.; Fenton, K. R.; Zavadil, K. R.; Tyliszczak, T.; Lai, W.; McCarty, K. F. Intercalation Pathway in Many-Particle $LiFePO_4$ Electrode Revealed by Nanoscale State-of-Charge Mapping. *Nano Lett.* **2013**, *13*, 866–872.
37. Orikasa, Y.; Maeda, T.; Koyama, Y.; Murayama, H.; Fukuda, K.; Tanida, H.; Arai, H.; Matsubara, E.; Uchimoto, Y.; Ogumi, Z. Direct Observation of a Metastable Crystal Phase of $Li_xFePO_4$ under Electrochemical Phase Transition. *J. Am. Chem. Soc.* **2013**, *135*, 5497–5500.
38. Zhang, X.; van Hulzen, M.; Singh, D. P.; Brownrigg, A.; Wright, J. P.; van Dijk, N. H.; Wagemaker, M. Rate-Induced Solubility and Suppression of the First-Order Phase Transition in Olivine $LiFePO_4$. *Nano Lett.* **2014**, *14*, 2279–2285.
39. Johannes, M. D.; Hoang, K.; Allen, J. L.; Gaskell, K. Hole Polaron Formation and Migration in Olivine Phosphate Materials. *Phys. Rev. B* **2012**, *85*, 115106.
40. Lee, J.; Zhou, W.; Idrobo, J. C.; Pennycook, S. J.; Patelides, S. T. Vacancy-Driven Anisotropic Defect Distribution in the Battery-Cathode Material $LiFePO_4$. *Phys. Rev. Lett.* **2011**, *107*, 085507.
41. Chung, S.-Y.; Choi, S.-Y.; Lee, S.; Ikuhara, Y. Distinct Configurations of Antisite Defects in Ordered Metal Phosphates: Comparison between $LiMnPO_4$ and $LiFePO_4$. *Phys. Rev. Lett.* **2012**, *108*, 195501.
42. Gu, L.; Zhu, C.; Li, H.; Yu, Y.; Li, C.; Tsukimoto, S.; Maier, J.; Ikuhara, Y. Direct Observation of Lithium Staging in Partially Delithiated $LiFePO_4$ at Atomic Resolution. *J. Am. Chem. Soc.* **2011**, *133*, 4661–4663.
43. Zhu, C.; Gu, L.; Suo, L.; Popovic, J.; Li, H.; Ikuhara, Y.; Maier, J. Size-Dependent Staging and Phase Transition in $LiFePO_4$/$FePO_4$. *Adv. Funct. Mater.* **2014**, *24*, 312–318.
44. Truong, Q. D.; Devaraju, M. K.; Sasaki, Y.; Hyodo, H.; Tomai, T.; Honma, I. Relocation of Cobalt Ions in Electrochemically Delithiated $LiCoPO_4$ Cathode Materials. *Chem. Mater.* **2014**, *26*, 2770–2773.
45. Hÿtch, M. J.; Snoeck, E.; Kilaas, R. Quantitative Measurement of Displacement and Strain Fields from HREM Micrographs. *Ultramicroscopy* **1998**, *74*, 131–146.
46. Feigin, L. A.; Svergun, D. I. *Structure Analysis by Small-Angle X-ray and Neutron Scattering*; Plenum Press: New York, 1987.
47. Bartlett, P.; Ottewill, R. H. A Neutron Scattering Study of the Structure of a Bimodal Colloidal Crystal. *J. Chem. Phys.* **1992**, *96*, 3306–3318.
48. Kline, S. R. Reduction and Analysis of SANS and USANS Data using IGOR Pro. *J. Appl. Crystallogr.* **2006**, *39*, 895–900.
49. Wang, L.; Zhou, F.; Meng, Y. S.; Ceder, G. First-Principles Study of Surface Properties of $LiFePO_4$: Surface Energy, Structure, Wulff Shape, and Surface Redox Potential. *Phys. Rev. B* **2007**, *76*, 165435.
50. Dixit, H.; Zhou, W.; Idrobo, J.-C.; Nanda, J.; Cooper, V. R. Facet-Dependent Disorder in Pristine High-Voltage Lithium−Manganese-Rich Cathode Material. *ACS Nano* **2014**, *8*, 12710–12716.
51. Mei, R.; Song, X.; Yang, Y.; An, Z.; Zhang, J. Plate-Like $LiFePO_4$ Crystallite with Preferential Growth of (010) Lattice Plane for High Performance Li-Ion Batteries. *RSC Adv.* **2014**, *4*, 5746–5752.